THE JOURNAL OF PHYSICAL CHEMISTRY LETTERS
A JOURNAL OF THE AMERICAN CHEMICAL SOCIETY

pubs.acs.org/JPCL Letter

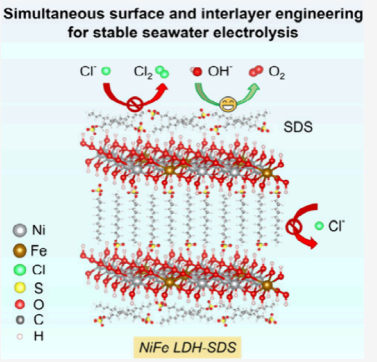
Simultaneous Surface and Interlayer Engineering of NiFe LDH via a Facile Anionic Surfactant Incorporation for Stable Ampere-Level Seawater Oxidation

Vahid Daneshvariesfahlan, Yifei Xu, Shengyu Ma, Ping Xu,* Qiang Fu, Yuming Huang, Bing Zhang, Mir Ghasem Hosseini,* Jiheng Zhang, Yishen Cheng, Kaixi Wang,* and Bo Song*

Cite This: J. Phys. Chem. Lett. 2026, 17, 4828−4838 Read Online

ACCESS | Metrics & More | Article Recommendations | Supporting Information

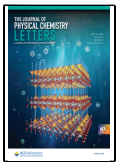
ABSTRACT: Ampere-level direct seawater electrolysis offers a sustainable approach for green hydrogen production, but its advancement is hindered by the competitive chloride evolution reaction (ClER) and catalyst corrosion at the anode. To overcome this limitation, we herein demonstrate a simultaneous surface and interlayer engineering of NiFe layered double hydroxide (LDH) anode by incorporating anionic surfactant (sodium dodecyl sulfate, SDS) through a facile anion exchange strategy. The dodecyl sulfate (DS) anion intercalation significantly expands the interlayer spacing and modulates the electronic structure of metal centers, thereby enhancing the intrinsic oxygen evolution reaction (OER) activity. Concurrently, the anionic groups anchored in the interlayer and adsorbed on the surface create a persistent electrostatic barrier that effectively repels Cl^- ions. Consequently, NiFe LDH-SDS achieves 1.0 A cm^{-2} at low overpotentials of 311 mV and 353 mV in alkaline simulated and natural seawater, respectively, and delivers exceptional corrosion resistance and durability, operating stably for over 500 h in simulated and 380 h in natural seawater at 1.0 A cm^{-2}, which far outperforms pristine NiFe LDH. More impressively, it sustains consistent performance for 500 h in overall seawater splitting at 1.0 A cm^{-2}. This work offers a facile route to develop corrosion-resistant OER electrocatalysts for seawater splitting.



The worldwide shift toward sustainable energy has brought hydrogen into sharp focus as a high-energy-density fuel carrier with zero emissions.[1−6] Currently, hydrogen production remains heavily reliant on fossil fuels, resulting in significant CO_2 emissions.[7,8] While renewable energy-driven water electrolysis offers a promising alternative, its current dependence on pure water presents a critical dilemma that large-scale implementation would inevitably exacerbate the growing scarcity of freshwater supplies.[9] Seawater electrolysis thus emerges as an attractive solution, leveraging its natural abundance and high ionic conductivity up to 10^6 times that of pure water, which substantially reduce Ohmic losses and enhances energy efficiency for large-scale operations.[10] Nevertheless, direct seawater electrolysis presents considerable difficulties due to its diverse chemical matrix. At the anode, the desired oxygen evolution reaction (OER) must compete with the kinetically favored chlorine evolution reaction (ClER), while chloride-induced corrosion mechanisms further degrade catalyst performance.[11] Although alkaline conditions thermodynamically favor OER over hypochlorite formation (with a ∼490 mV lower onset potential), industrial high-current-density operation introduces substantial overpotentials that promote parasitic hypochlorite generation. These competing reaction pathways collectively reduce Faradaic efficiency and severely compromise long-term operational stability in seawater environments.[12−15]

Overcoming these challenges requires the development of anode catalysts that achieve superior catalytic activity and robust chloride tolerance. A dual-approach framework is therefore proposed to advance both the efficiency and durability of seawater oxidation anodes. First, engineering the local microenvironment to electrostatically repel chloride via anion-rich surfaces, Lewis-acidic sites, and a dense negative charge network. Second, modifying the catalyst surface through coordination chemistry, where adsorbed molecular modifiers tune the electronic structure of active metal centers, intrinsically reinforcing chloride rejection.[16] In this regard, constructing a chloride-repelling interface, typically through in situ-generated oxyanions or preattached species, represents a direction actively pursued by several research groups.[17,18] For example, catalysts like NiFe/NiS,[19] RuMoNi,[20] and CoFe PBA/Co_2P,[21] undergo surface reconstruction under OER conditions, releasing functional anions such as SO_4^{2-}, MoO_4^{2-}, PO_4^{3-}, and $Fe(CN)_6^{3-}$. These anionic species adsorb

Received: January 7, 2026
Revised: February 26, 2026
Accepted: March 3, 2026
Published: March 9, 2026



Downloaded via CHULALONGKORN UNIV on June 2, 2026 at 06:44:08 (UTC).
See https://pubs.acs.org/sharingguidelines for options on how to legitimately share published articles.

ACS Publications © 2026 American Chemical Society

https://doi.org/10.1021/acs.jpclett.6c00056
J. Phys. Chem. Lett. 2026, 17, 4828−4838

onto the catalyst surface and create a localized negative layer, repelling Cl^- ions and mitigating corrosion. An alternative design incorporates stable anionic molecules, such as polyoxometalates (POMs),[18] which are anchored to specific sites on catalysts like CoFe hydroxide. This design actively repels Cl^- while promoting the desired oxygen evolution. In addition, protective coatings such as graphene oxide[22] or graphene quantum dots[23] have been applied to catalyst surfaces to block chloride ions via electrostatic interactions. Despite their effectiveness in seawater oxidation, many of these designs rely on multistep syntheses or delicate architectures, making large-scale production challenging.[24] Alternatively, electrolyte engineering, which involves adjustments to electrolytic composition, provides another route to mitigate chloride corrosion. The introduction of specific additives, including sulfate,[25] carbonate,[26] fluoride,[24] and hexafluorophosphate (PF_6^-),[27] has been demonstrated to substantially enhance anode stability. For instance, incorporating F^- ions into the electrolyte can enhance OER performance by altering the electronic structure of active sites and establishing a local microenvironment that favors OH^- transport over Cl^- intrusion.[24]

Layered double hydroxides (LDHs) are considered highly promising anode catalysts for seawater oxidation because of their unique layered structures, flexible composition, and cost-effectiveness.[28−30] However, their activity and durability are constrained by limited active site accessibility and poor chloride corrosion resistance.[31,32] Intercalating anions between LDH layers to expand the interlamellar spacing has been proven an effective strategy for improving catalytic activity.[33] Although the aforementioned electrolyte engineering approach can significantly enhance corrosion resistance through anion intercalation and surface adsorption, small-molecule anionic additives can barely widen the interlayer gap, hindering the utilization of interlayer active sites. Recent studies indicate that macromolecular intercalants can induce a more pronounced expansion of the interlayer spacing, leading to faster ion diffusion and better electrochemical performance.[31] Inspired by these insights, the incorporation of large anionic surfactants into the interlayers of LDH may represent a compelling strategy. This approach not only widen the interlayer spacing to boost seawater oxidation activity but also utilizes the electrostatic repulsion to block Cl^- diffusion and corrosion within the interlayers. Simultaneously, the surfactant anions adsorbed onto the LDH surface can generate a protective layer, further strengthening the chloride resistance.

In this work, we employed sodium dodecyl sulfate (SDS) as a large intercalant to achieve simultaneous surface and interlayer engineering of NiFe LDH for stable ampere-level seawater oxidation. The SDS-modified NiFe LDH (denoted as NiFe LDH-SDS) was prepared via a straightforward interlayer anion exchange process. The dodecyl sulfate (DS) anion insertion significantly expands the interlayer distance, which not only exposes more active sites but also subtly tunes the electronic states of metal centers, leading to promoted intrinsic OER property. At the same time, the negatively charged sulfate groups anchored within the interlayer and adsorbed on the surface establish an electrostatic barrier that effectively repels Cl^- ions, dramatically improving corrosion resistance. When tested in alkaline seawater electrolyte, the NiFe LDH-SDS catalyst demonstrates exceptional catalytic activity, achieving a current density of 1.0 A cm^{-2} with minimal overpotentials of just 311 mV (simulated seawater) and 353 mV (natural seawater). More notably, it sustains stable operation in an overall alkaline seawater electrolysis for 500 h at 1.0 A cm^{-2}, showcasing unprecedented durability for practical applications.

Figure 1a illustrates the modification of NiFe LDH catalysts by SDS through a facile anion-exchange method. First, self-

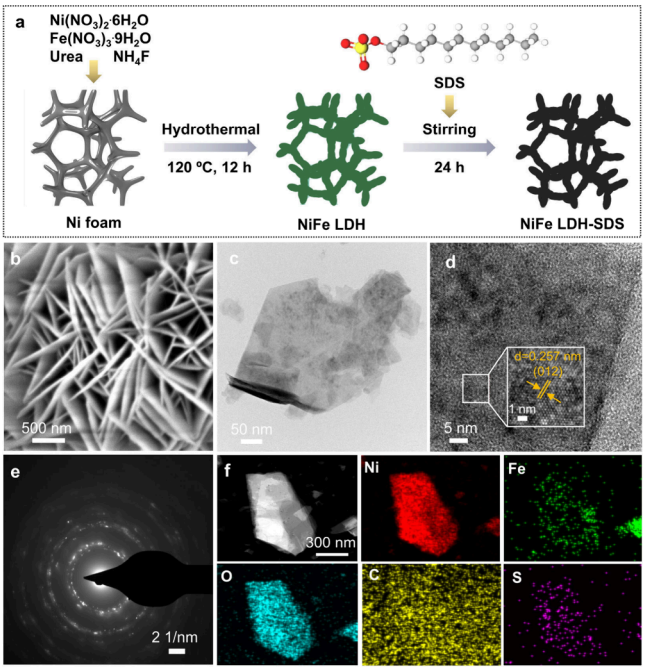


Figure 1. Preparation method and morphological analysis of NiFe LDH-SDS. (a) Schematic of the preparation procedure. (b) High-magnification SEM image. (c) TEM image. (d) HR-TEM image. (e) Corresponding SAED pattern. (f) Elemental mapping for Ni, Fe, O, C, and S.

supported NiFe LDH nanostructures were hydrothermally grown on a precleaned Ni foam substrate. Subsequently, the prepared NiFe LDH was subjected to an anion exchange process to intercalate DS anions into its interlayer spaces, yielding the final NiFe LDH-SDS electrode. Low-magnification scanning electron microscopy (SEM) images shown in Figure S1a,b for NiFe LDH-SDS and Figure S2a,b for NiFe LDH clearly illustrate the uniform distribution, continuity, and total coverage of the catalyst on the surfaces of the porous nickel foam support, providing strong evidence of the successful preparation process. High-magnification SEM images (Figure 1b and Figure S2c) display vertically aligned two-dimensional nanosheets grown on the Ni foam for both pristine NiFe LDH and the NiFe LDH-SDS. No significant morphological change after SDS modification indicates that the ion-exchange process does not disrupt the nanosheet architecture, thereby preserving the structural integrity of the NiFe LDH. The nanosheet morphology was further verified using transmission electron microscopy (TEM) (Figure 1c and Figure S2d), which reveals a sheet-like and semitransparent morphology for both NiFe LDH and NiFe LDH-SDS.[34,35] High-resolution TEM (HR-TEM) images confirm the crystalline structure of NiFe LDH-SDS (Figure 1d) and NiFe LDH (Figure S2e), with measured lattice fringes exhibiting *d*-spacings of 0.257 and 0.254 nm, respectively. These values are attributed to the (012) crystallographic plane of NiFe LDH (see Figure S3 for further details).[36] The selected-area electron diffraction (SAED) patterns for both samples (Figure 1e and Figure S2f) exhibit

https://doi.org/10.1021/acs.jpclett.6c00056
J. Phys. Chem. Lett. 2026, 17, 4828−4838

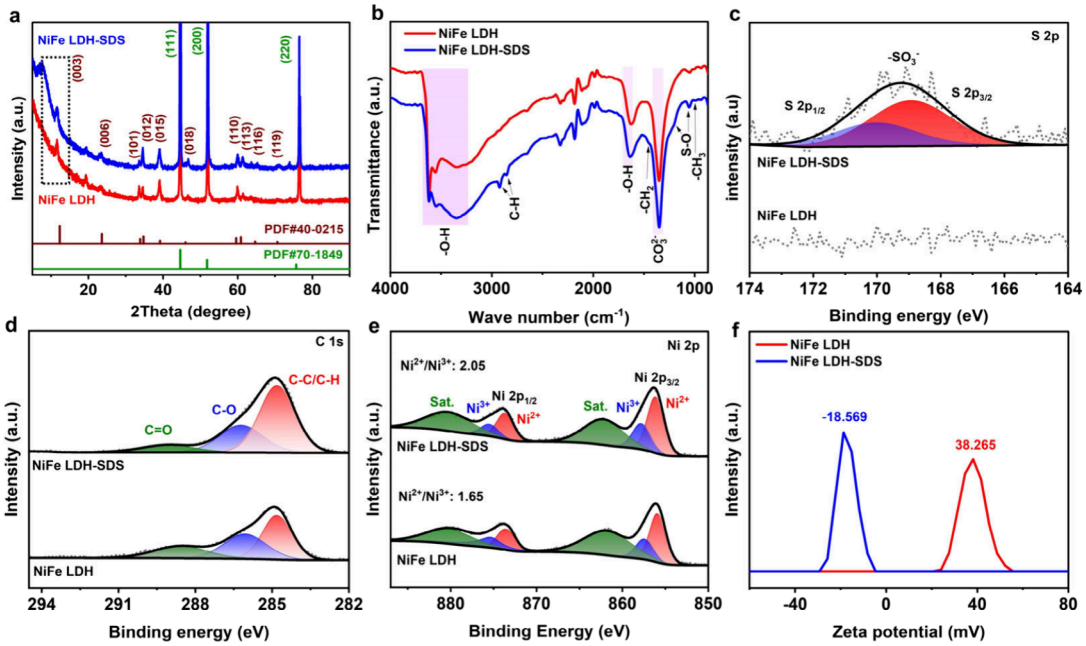


Figure 2. Phase and composition characterization of prepared catalysts. (a) XRD pattern. (b) FTIR spectra. High-resolution XPS spectra of (c) S 2p, (d) C 1s, and (e) Ni 2p. (f) Zeta potential analysis.

distinct rings rather than sharp spots, confirming their polycrystalline nature.[33] Furthermore, Energy dispersive X-ray (EDX) elemental mappings reveal a homogeneous dispersion of Ni, Fe, O, C, and S throughout the NiFe-LDH-SDS nanosheets (Figure 1f), suggesting the introduction of DS anions into the structure.

X-ray diffraction (XRD) was carried out to probe the crystal structure of the as-synthesized samples. As illustrated in Figure 2a, both NiFe LDH and NiFe LDH-SDS display the same set of strong diffraction peaks at 44.6°, 51.9°, and 76.5°, which originate from the metallic nickel foam substrate (PDF#04−0850).[37] In addition, the XRD pattern of pristine NiFe LDH reveals distinct reflections consistent with iron nickel carbonate hydroxide hydrate (PDF#40−0215),[36] verifying the successful synthesis of NiFe LDH. Following SDS modification, a new diffraction peak emerges at 6.96° for NiFe LDH-SDS, which can be attributed to the expanded (003) plane of pristine NiFe LDH.[33] According to Bragg's law, this peak corresponds to an interlayer spacing of 1.27 nm, a significant expansion from 0.77 nm (2θ = 11.52°) in the NiFe LDH. After accounting for the 0.48 nm thickness of host layers, the observed gallery expansion of 0.79 nm provides clear evidence for the successful intercalation of DS anions into the interlayer of NiFe LDH.[33]

Fourier-transform infrared (FTIR) spectroscopy was employed to further prove the successful incorporation of DS anions into the NiFe LDH interlayer. As shown in Figure 2b, both samples share common bands indicative of the LDH structure, comprising a strong band at ∼ 3500 cm^{-1} from O−H stretching of water molecules confined within the interlayers, a band at 1645 cm^{-1} from H−O−H bending mode of water, and a band at 1355 cm^{-1} assigned to antisymmetric stretching vibration of CO_3^{2-} anions.[38] In addition, the NiFe LDH-SDS exhibits distinct new vibrational bands that are absent in the NiFe LDH, including the asymmetric and symmetric C−H stretches of the SDS alkyl chain at 2922 cm^{-1} and 2850 cm^{-1}, the $-CH_2$ scissoring mode at 1465 cm^{-1}, the $-CH_3$ deformation mode at 980 cm^{-1}, and S═O stretching bands at 1050 cm^{-1} and 1190 cm^{-1}.[39−41] The origin of these bands is confirmed by comparison with the FTIR spectrum of pure SDS, provided in Figure S4. The presence of the SDS-specific bands, concurrent with the attenuation of the carbonate band, confirms that DS anions have partially replaced the CO_3^{2-} anions within the interlayer space, verifying successful intercalation.

The surface chemistry and electronic structure of both catalysts were studied through X-ray photoelectron spectroscopy (XPS). The survey spectrum of NiFe LDH-SDS in Figure S5a reveals the presence of the S 2p peak, which is absent in the pristine NiFe LDH. The high-resolution S 2p spectrum (Figure 2c) of NiFe LDH-SDS exhibits a distinct doublet with peaks at 168.9 eV (S $2p_{3/2}$) and 170.0 eV (S $2p_{1/2}$). These observed peaks match those reported for the $-SO_3^-$ group of SDS.[42−44] Further evidence comes from the C 1s region. As shown in Figure 2d, the C 1s spectra are divided into three distinct chemical states. The peak at the binding energy of 288.9 eV is a definitive marker for the carbonyl (C═O) group, and the peaks at 284.8 and 286.0 eV correspond to the C−C/C-H and C−O bonds, respectively. Following SDS intercalation, the C═O intensity drops noticeably, while the C−C/C−H component grows substantially (Table S1), which is related to the long alkyl group of the intercalated DS anions. These changes in the carbon environment confirm the partial replacement of carbonate by SDS within the LDH interlayer,[38] corroborating the structural evidence obtained from FTIR. The deconvoluted Ni 2p spectrum in Figure 2e displays the spin−orbit doublet consisting of the Ni $2p_{3/2}$ and Ni $2p_{1/2}$ peaks and their satellites for both catalysts. The Ni^{2+}/Ni^{3+} ratio increases from 1.65 to 2.05 following anion exchange with DS (Table S2), reflecting the replacement of CO_3^{2-} by the lower charge density of DS.[27,33] For the Fe 2p spectra (Figure S5b), the observed positive shift in the binding energy of the Fe $2p_{3/2}$ peaks following SDS intercalation may be attributed to the presence of new chemical bonds at the SDS-Fe interface.[27] The O 1s XPS spectra of both catalysts are deconvoluted into three

https://doi.org/10.1021/acs.jpclett.6c00056
J. Phys. Chem. Lett. 2026, 17, 4828−4838

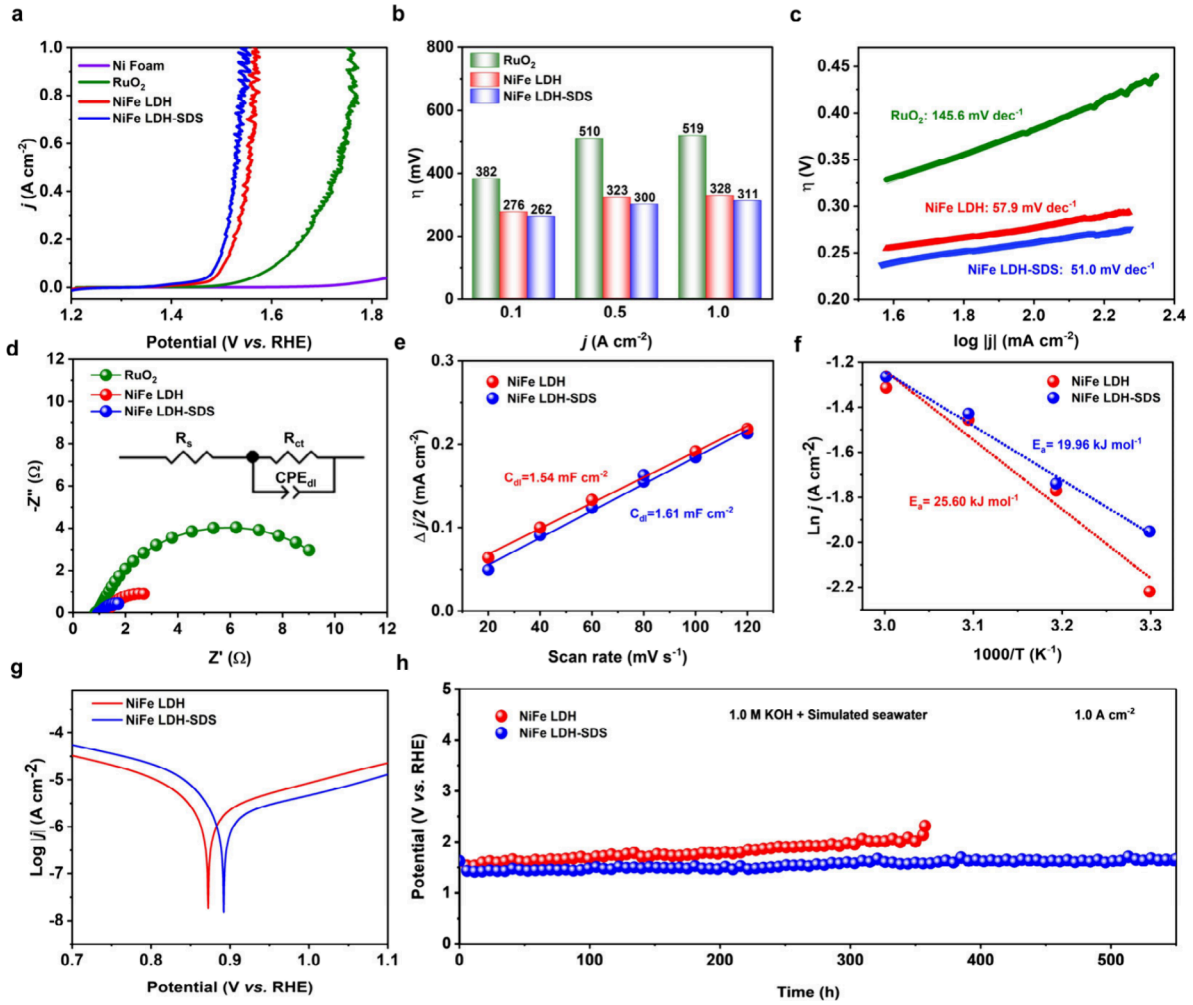


Figure 3. Comprehensive evaluation of the OER performance for the synthesized catalysts in an alkaline simulated seawater electrolyte. (a) iR_s-corrected LSV curves. (b) Overpotential values at various current densities. (c) Corresponding Tafel plots. (d) Nyquist plots with an equivalent circuit. (e) Scan rate dependence of the capacitive current at 1.2 V (vs. RHE). (f) Arrhenius plot for activation energy. (g) Corrosion Tafel polarization plots. (h) Chronoamperometric measurement at 1 A cm^{-2}.

components: 530.8 eV (metal−oxygen, M-O), 531.6 eV (metal-hydroxide, M−OH), and 533.1 eV (adsorbed H_2O) (Figure S5c).[37] The high intensity of the M−OH signal suggests a metal hydroxide-dominated composition.

Zeta potential was measured to characterize the change in surface charge upon the modification of NiFe LDH with SDS. As shown in Figure 2f, the average zeta potential shifted significantly from 38.265 mV to −18.569 mV following SDS incorporation. This marked transition signifies a substantial increase in negative charge on the modified electrode surface, corroborating the successful incorporation of SDS.[45,46] The negatively charged interface establishes a repulsive electrostatic environment that hinders the adsorption of Cl^- ions onto the catalyst surface, which is conducive to the improvement of both corrosion resistance and catalytic durability. In addition, scaling water electrolysis at high current densities is often constrained by kinetic mass transport at the electrode−electrolyte interface, a process strongly governed by electrode wettability. To assess this property, we performed dynamic contact angle measurements employing alkaline simulated seawater droplets (1.0 M KOH + 0.5 M NaCl). As shown in Figure S6, the as-prepared NiFe LDH-SDS exhibits super-hydrophilicity, causing an electrolyte droplet to spread quickly, whereas the Ni foam electrode remains distinctly hydrophobic with a large contact angle. The enhanced hydrophilicity of NiFe LDH-SDS facilitates charge transfer and ensures rapid electrolyte refreshment at the interface under demanding catalytic conditions.[47]

The OER activity of the synthesized electrocatalysts was first examined in an alkaline simulated seawater electrolyte using a typical three-electrode cell. The linear sweep voltammetry (LSV) polarization curves in Figure 3a demonstrate that the NiFe LDH-SDS (prepared at the optimal SDS concentration, Figure S7) exhibits better OER activity than NiFe LDH and significantly outperforms both the RuO_2 and Ni foam electrodes. As illustrated in Figure 3b, the incorporation of SDS lowers the overpotentials required to achieve current densities of 0.1, 0.5, and 1.0 A cm^{-2} (262, 300, and 311 mV) compared to the corresponding values of 276, 323, and 328 mV for pristine NiFe LDH. For RuO_2, it requires larger overpotentials of 382, 510, and 519 mV to obtain the same current densities. The enhanced OER activity is further reflected in the Tafel analysis. As depicted in Figure 3c, among the synthesized catalysts, NiFe LDH-SDS exhibits a Tafel slope of 51.0 mV dec^{-1}, which is lower than that of NiFe LDH (57.9 mV dec^{-1}) and significantly lower than that of

https://doi.org/10.1021/acs.jpclett.6c00056
J. Phys. Chem. Lett. 2026, 17, 4828−4838

RuO_2 (145.6 mV dec^{-1}). This trend indicates more favorable OER kinetics and enhanced electrocatalytic efficiency for NiFe LDH-SDS.[48] Electrochemical impedance spectroscopy (EIS) was conducted to probe the interfacial reactions kinetics. The Nyquist plots in Figure 3d were fitted using the Randles equivalent circuit (inset). This model consists of a solution resistance (R_s), a charge-transfer resistance (R_{ct}), and a constant phase element representing the double layer (CPE_{dl}). The corresponding fitting parameters are summarized in Table S3. The results show that NiFe LDH-SDS exhibits the smallest semicircle diameter and the lowest R_{ct} (2.266 Ω), outperforming both NiFe LDH (2.887 Ω) and RuO_2 (10.740 Ω), indicating the accelerated interfacial electron transfer.

To determine the electrochemical surface area (ECSA), the double-layer capacitance (C_{dl}) of the synthesized catalysts was measured via cyclic voltammetry (CV) within the nonfaradaic potential window (Figure S8). As illustrated in Figure 3e, the C_{dl} of NiFe LDH-SDS is slightly higher than that of NiFe LDH. This finding aligns with the larger ECSA of 40.25 cm^2 for NiFe LDH-SDS, compared to 38.50 cm^2 for NiFe LDH (Figure S9a). This suggests that NiFe LDH-SDS has a higher density of accessible active sites. Furthermore, even after normalizing the current to the ECSA, NiFe LDH-SDS maintains a higher specific activity than NiFe LDH (Figure S9b), confirming its superior intrinsic catalytic performance. This activity trend remains consistent when the current is normalized by geometrical surface area, as shown in Figure 3a. The intrinsic OER activity of the synthesized catalysts was further determined in simulated seawater through activation energy (E_a) determination. As an intrinsic property, E_a provides a direct measure of inherent catalytic efficiency, independent of extrinsic factors such as surface area.[49] The E_a was determined by applying the Arrhenius equation to current densities obtained from LSV at a fixed overpotential (400 mV) across various temperatures (Figure S10). The current density (j) is directly related to the rate constant (k) in electrocatalytic reactions. Therefore, based on the Arrhenius relationship ($k = Ae^{-E_a/RT}$), where A is the pre-exponential factor, R is the ideal gas constant, and T is the temperature, a linear correlation exists between $\ln(j)$ and 1/T. The E_a was subsequently derived from the slope of this plot.[50,51] As depicted in Figure 3f, the NiFe LDH-SDS catalyst exhibits an E_a of 19.96 kJ mol^{-1}, substantially lower than that of NiFe LDH (25.60 kJ mol^{-1}). This lower activation energy implies a diminished energy barrier for OER, demonstrating that SDS incorporation enhances the intrinsic activity of the pristine NiFe LDH.

In chloride-rich environments, the long-term electrochemical stability hinges critically on the corrosion resistance of catalysts. To assess this, Tafel polarization measurements were performed in a simulated seawater electrolyte.[25,52] As shown in Figure 3g and Table S4, the incorporation of SDS into the NiFe LDH structure improved its corrosion resistance, which is evidenced by a decrease in the exchange current density (j_0) from 2.26×10^{-6} A cm^{-2} to 1.86×10^{-6} A cm^{-2} and an increase in the corrosion potential (E_{corr}) from 0.87 to 0.90 V. This behavior can be traced to the negatively charged interface generated on the NiFe LDH-SDS by SDS incorporation, effectively shielding the DS anions from anion exchange with Cl^- in the electrolyte.[33] For more details, the Cl 2p XPS spectra of NiFe LDH-SDS and NiFe LDH were evaluated after a continuous operation of 6 h at a current density of 1.0 A cm^{-2} to investigate the differential adsorption characteristics of Cl^- on the electrodes. Figure S11 shows reduced Cl^- adsorption on the NiFe LDH-SDS compared to the NiFe LDH electrode. This observation indicates that the negatively charged surface layer of the NiFe LDH-SDS electrode hinders the interaction and subsequent adsorption of Cl^- ions onto the electrode surface and decreases Cl-induced corrosion.[53,54]

Practical deployment of electrocatalysts in seawater demands excellent durability at ampere-level current densities under aggressive anodic conditions. Therefore, the long-term stability of NiFe LDH-SDS was evaluated and compared to NiFe LDH via chronopotentiometry at 1.0 A cm^{-2} in simulated seawater. As can be seen in Figure 3h, the NiFe LDH-SDS catalyst demonstrates exceptional stability, maintaining stable operation for over 550 h at 1.0 A cm^{-2}, with a potential increase of less than 30 mV. The minor periodic fluctuations observed in the stability curve stem from diurnal temperature variations and water replenishment cycles. In sharp contrast, the NiFe LDH electrode degraded rapidly, suffering a potential surge by more than 500 mV after only 350 h. This failure is visually evident, as the NiFe LDH catalyst after stability test shows obvious physical damage in the optical image (Figure S12a), whereas its SDS-modified counterpart remains structurally intact (Figure S12e). The superior durability of NiFe LDH-SDS was further corroborated by the post-test SEM images (Figure S12b-d,f–h), which revealed a better-preserved morphology compared to pristine NiFe LDH. Table S5 compares the stability of the DS anion-boosted strategy with other anion-based Cl^--repelling strategies, confirming the superior durability of our modified catalyst for seawater electrolysis.[25,31,55−58] Moreover, the post-XPS analysis reveals that the Ni^{2+}/Ni^{3+} ratio decreases after the stability test for both samples (Figure 4a and Table S6). However, this reduction in NiFe LDH-SDS is more pronounced, indicating the formation of more catalytically active oxyhydroxide. The Fe 2p spectra show a similar trend (Figure S13 and Table S6), reinforcing this conclusion. ICP-OES analysis of electrolytes after stability test reveals that the leaching amounts of both Ni and Fe from NiFe LDH-SDS are substantially diminished relative to NiFe LDH (Figure 4b and Table S7), confirming the improved structural stability of NiFe LDH after SDS incorporation. In addition, the interaction of water molecules and $-SO_3^-$ on the catalyst surface during electrolysis creates a hydrogen-bonded, semipermeable framework. This structure selectively blocks Cl^- ions, which are poor hydrogen-bond acceptors, while permitting the free diffusion of OH^- ions. Consequently, the NiFe LDH-SDS electrode achieves enhanced durability and corrosion resistance without compromising its catalytic activity.[59]

Raman spectroscopic analysis of the NiFe-LDH following SDS incorporation exhibits a marked blue shift in the characteristic $Ni(OH)_2$ vibrational modes (Figure S14). The signal associated with the CO_3^{2-} species (727.59 cm^{-1}) in NiFe LDH is significantly weakened after SDS incorporation, further proving successful preparation of NiFe LDH-SDS.[27] Furthermore, in situ Raman spectroscopy was employed to investigate the dynamic evolution of the catalyst surface in alkaline simulated seawater (Figure S15). A key spectral change emerged with increasing applied potential. For NiFe LDH (Figure 4c and 4d), a phase transition occurred at 1.4 V vs RHE: the peaks at ∼460 and ∼530 cm^{-1}, attributed to the Ni−O and Fe−O vibrations of the pristine LDH phase, shifted to an active NiOOH phase. This transformation is indicated by

https://doi.org/10.1021/acs.jpclett.6c00056
J. Phys. Chem. Lett. 2026, 17, 4828−4838

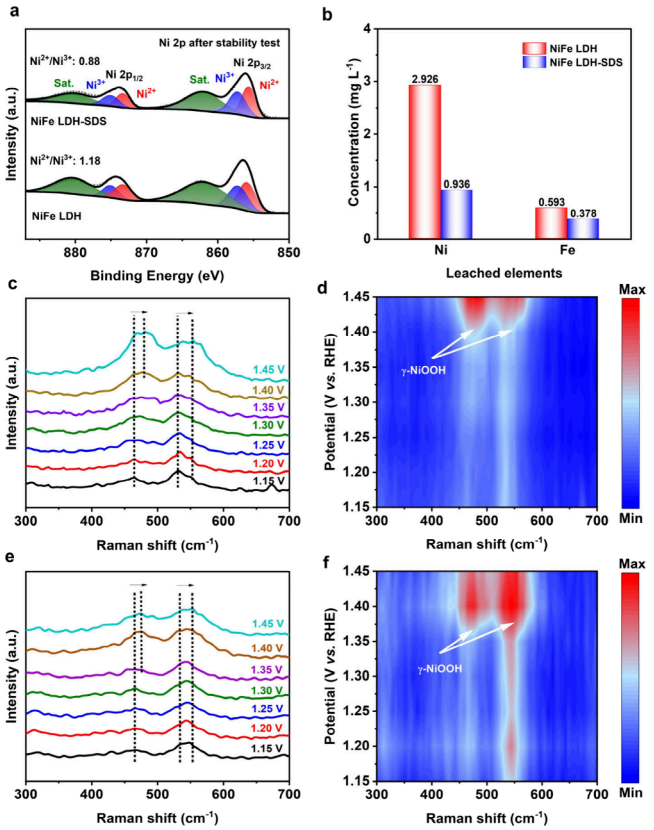


Figure 4. (a) Ni 2p XPS spectra for NiFe LDH-SDS and NiFe LDH after stability. (b) Measured concentrations of leached Ni and Fe ions via ICP-OES. In situ Raman analysis in alkaline simulated seawater for (c,d) NiFe LDH and (e,f) NiFe LDH-SDS, demonstrating (c,e) the recorded spectra and (d,f) their derived contour maps across a potential range of 1.15 to 1.45 V (vs. RHE).

the emergence of new peaks at 488 and 569 cm^{-1}, characteristic of γ-NiOOH and Fe-doped γ-NiOOH, respectively.[60,61] This transformation, entailing a nickel valence transition to a mixed Ni^{3+}/Ni^{4+}, was observed at a lower potential of 1.35 V vs RHE for NiFe LDH-SDS (Figure 4e and 4f). This earlier onset of active phase formation at lower overpotential is a critical factor in the enhanced OER performance of the SDS-modified catalyst.[60]

To assess real-world applicability, the OER performance of NiFe LDH-SDS was evaluated in alkaline natural seawater (1.0 M KOH + seawater), with the seawater sourced from Macau, China (22.10° N, 113.32° E) (Figure S16). As evidenced by the LSV curves (Figure 5a), the NiFe LDH-SDS electrode exhibits enhanced electrocatalytic activity relative to the pristine NiFe LDH, requiring lower overpotentials of 282, 333, and 343 mV to deliver current densities of 0.1, 0.5, and 1.0 A cm^{-2}, respectively. In contrast, the NiFe LDH requires overpotentials of 291, 345, and 364 mV to attain equivalent current densities. This enhanced performance, manifested in both simulated and natural seawater electrolytes, underscores the efficacy of the SDS incorporation. Benchmarking against recent literature in alkaline natural seawater (Figure 5b, Table S8) show that our catalyst outperforms most reported catalysts, highlighting its practical potential.[15,48,56,62−67] Furthermore, the chronopotentiometry measurements (Figure 5c) demonstrate the superior stability of NiFe LDH-SDS, which maintains its catalytic operation for over 380 h at 1 A cm^{-2}. This extended lifetime significantly surpasses the unmodified NiFe LDH, which fails within 240 h, and positions our catalyst competitively among other leading materials, as supported by the comparative analysis in Figure 5d and Table S8.[15,48,56,62−67] Moreover, the generation of corrosive chloride oxidation byproducts (e.g., hypochlorite, ClO^-) during OER was monitored using an iodide titration method, wherein hypochlorite formation is qualitatively identified by the emergence of a yellow color.[15] As shown in Figure S17, the electrolyte surrounding the NiFe LDH-SDS catalyst remains nearly colorless after prolonged electrolysis, in stark contrast to the significant change observed with NiFe LDH. This finding confirms the effective suppression of reactive chlorine species and directly demonstrates the superior OER selectivity of NiFe LDH-SDS in seawater electrolyte compared to the pristine counterpart.

To assess the system-level performance of NiFe LDH-SDS, overall seawater splitting was performed in a two-electrode configuration by employing NiFe LDH-SDS as the anode and commercial 20% Pt/C as the cathode (denoted as NiFe LDH-SDS||Pt/C). As illustrated in the polarization curve (Figure 5e), the resulting cell exhibits excellent performance in a 1.0 M KOH + seawater electrolyte, requiring low voltages of 1.66, 1.91, and 1.99 V to deliver 0.1, 0.5, and 1.0 A cm^{-2}, respectively. In comparison, the NiFe LDH||Pt/C system requires higher voltages to obtain the same current densities (Figure S18a). In addition, the electrolyzer exhibits impressive long-term stability, with minimal performance degradation observed during 500 h of continuous operation at 1.0 A cm^{-2}. This performance exceeds the typical 190-h limit seen with pristine NiFe LDH anodes (Figure S18b), highlighting the exceptional durability and mechanical robustness of the NiFe LDH-SDS under demanding operational conditions. Direct benchmarking against state-of-the-art water electrolyzers (Table S9) confirms the practical competitiveness of our integrated NiFe LDH-SDS||Pt/C system. Our electrolyzer achieves a low operating voltage and demonstrates superior long-term stability compared to many recently reported alternatives.[20,22,54,58,64,68−72] Additionally, the OER Faradaic efficiency (FE) was calculated by measuring the evolved O_2 gas through the drainage method in an H-type electrolytic cell (Figure S19). The NiFe LDH-SDS catalyst achieves a superior OER FE of ~100% at 0.1 A cm^{-2} in alkaline seawater, which is maintained across different testing durations (Figure 5g), confirming its high selectivity and stability during electrolysis.[47,69]

In summary, this work develops a facile surfactant-assisted method to create highly corrosion-resistant NiFe LDH anodes for seawater oxidation. This approach substantially improves operational durability without compromising catalytic activity. The enhanced performance of NiFe LDH-SDS stems from an expanded interlayer space coupled with the negative surface and interlayer charges, which electrostatically repel Cl^- ions to inhibit the destructive anion exchange and structural degradation. Consequently, the optimized NiFe LDH-SDS shows superior OER electrocatalytic performance in alkaline simulated and natural seawater, which requires low overpotentials of 311 and 353 mV to sustain 1.0 A cm^{-2}, respectively. More critically, it demonstrates remarkable long-term stability, operating for over 500 h in alkaline simulated seawater and 380 h in alkaline natural seawater at 1.0 A cm^{-2}, significantly surpassing the prestine NiFe LDH. When integrated into a two-electrode electrolyzer with a Pt/C

https://doi.org/10.1021/acs.jpclett.6c00056
J. Phys. Chem. Lett. 2026, 17, 4828−4838

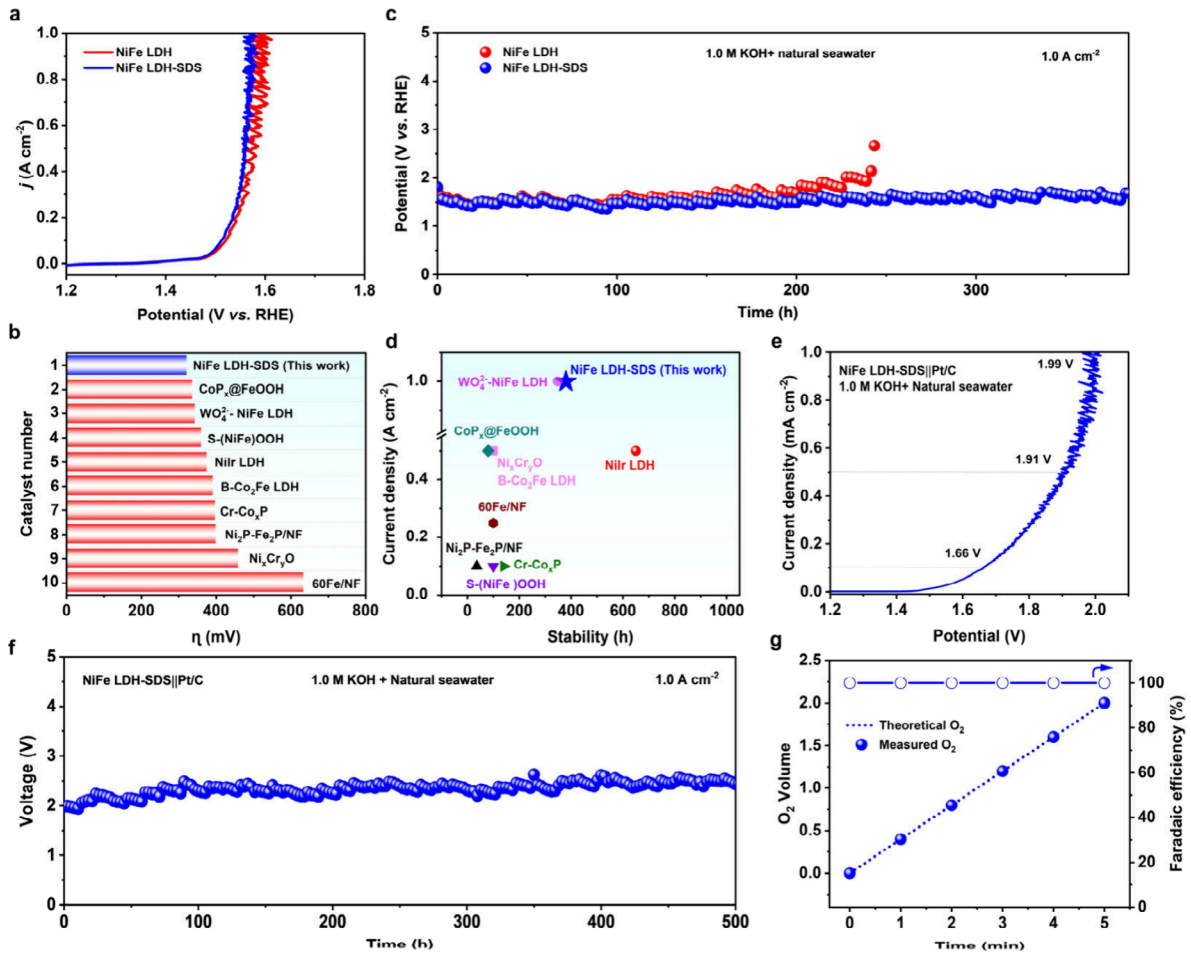


Figure 5. OER performance of the synthesized catalysts in an alkaline natural seawater electrolyte. (a) LSV curves. (b) Overpotential comparison of NiFe LDH-SDS with recently reported OER catalysts. (c) Chronoamperometric test at 1 A cm^{-2}. (d) Durability comparison of NiFe LDH-SDS with recently reported OER catalysts. Overall alkaline seawater splitting performance of the NiFe LDH-SDS||Pt/C two-electrode system in 1.0 M KOH + seawater: (e) Polarization curve and (f) Chronopotentiometry tests. (g) The amount of O_2 collected via the water drainage method as a function of time and the corresponding Faradaic efficiency for NiFe LDH-SDS.

cathode, the system requires low voltages of just 1.68, 2.03, and 2.22 V to reach 0.1, 0.5, and 1.0 A cm^{-2} in alkaline natural seawater, respectively, and operates continuously for 500 h without obvious degradation at 1.0 A cm^{-2}. This work provides a robust and practical framework for developing durable catalysts for industrial-scale hydrogen production from seawater.

METHODS

Materials

Nickel(II) nitrate hexahydrate ($Ni(NO_3)_2{\cdot}6H_2O$, Aladdin, ≥99.0%), iron(III) nitrate nonahydrate ($Fe(NO_3)_3{\cdot}9H_2O$, Aladdin, 98.5%), ammonium fluoride (NH_4F, Aladdin, ≥98.0%), urea ($CO(NH_2)_2$, Macklin reagent, 99.0%), ruthenium(IV) oxide (RuO_2, Aladdin, ≥99.9% metal basis), sodium dodecyl sulfate ($CH_3(CH_2)_{11}OSO_3Na$, Macklin reagent, 99.0%), ethanol (C_2H_5OH, Aladdin, ≥99.5%), isopropyl alcohol (C_3H_8O, Aladdin, ≥99.5%), acetone ($CO(CH_3)_2$, Aladdin, ≥99.5%), potassium hydroxide (KOH, Macklin reagent, ≥99.95%), sodium chloride (NaCl, Aladdin, ≥99.5%), hydrochloric acid (HCl, Sinopharm Chemical Reagent, 37.0%), potassium iodide (KI, Macklin reagent, 99.5%), sodium thiosulfate ($Na_2S_2O_3$, Macklin reagent, 99.0%), and sulfuric acid (H_2SO_4, Sinopharm Chemical Reagent, 98.0%) were utilized directly without further purification. Commercial materials included 20 wt % Pt/C and TGP-H-060 carbon paper (thickness 0.199 mm) were supplied by Suzhou Sinero Technology Co., Ltd. Nafion 117 solution (5.0%, D520) was bought from E. I. Dupont de Nemours and Company. 1.5 mm thick Nickel foam was acquired from Kunshan Jiayisheng Electronic Co., Ltd., and carefully prewashed with hydrochloric acid (3 M), ethanol, and acetone solutions, assisted by ultrasonication, to effectively eliminate the nickel oxide and hydrocarbons present on its surface. Natural seawater was collected from the waters of Macau, located in Macau, China (22.10° N, 113.32° E).

Preparation of NiFe LDH

A clear homogeneous solution was obtained via dissolution of 2.4 mmol $Ni(NO_3)_2{\cdot}6H_2O$, 0.8 mmol $Fe(NO_3)_3{\cdot}9H_2O$, 10.0 mmol urea, and 6.0 mmol NH_4F in 60.0 ml ultrapure water under vigorous stirring for 30 min. Next, a 1.5 cm × 4.0 cm piece of prewashed Ni foam was soaked in the solution. The mixture was sealed in a 100 mL Teflon-lined autoclave and subjected to a 12-h reaction at 120 °C. Upon reaching ambient temperature, the NiFe LDH on Ni foam with a loading of ~3.5 mg cm^{-2} was obtained by washing with ultrapure water and ethanol several times and drying in a vacuum oven at 60 °C overnight.

Preparation of NiFe LDH-SDS

Surfactant solutions were prepared at varying SDS concentrations (0.05−0.3 M) by dissolving a certain amount of surfactant in 100 mL of ultrapure water. The NiFe LDH on Ni foam was subsequently immersed in this solution and maintained for 24 h under a nitrogen atmosphere with vigorous stirring. Afterward, the modified NiFe LDH was removed from the solution, thoroughly rinsed copiously with DI

https://doi.org/10.1021/acs.jpclett.6c00056
J. Phys. Chem. Lett. 2026, 17, 4828−4838

water and ethanol, and then subjected to vacuum drying for 24 h. The prepared sample was labeled as NiFe LDH-SDS.

Preparation of RuO_2 Electrode

A uniform dispersion was obtained by ultrasonicating 5.0 mg of commercial RuO_2 powder in a mixed solvent of 0.97 mL of H_2O and ethanol (1:1) and 30 μL of Nafion 117 solution. Afterward, a certain amount of prepared ink was carefully dropped onto prewashed nickel foam (1 × 1 cm^2) and vacuum-dried at 60 °C for 12 h. The total mass loading of RuO_2 on the Ni foam was ~3.5 mg cm^{-2}.

Preparation of Pt/C Electrode

A uniform dispersion was obtained by ultrasonicating 15.0 mg of Pt/C (20 wt %) in a mixed solution of 3.52 mL of ultrapure water and isopropyl alcohol in a 1:3 ratio, along with 240 μL of Nafion 117 solution. The prepared ink was then loaded onto carbon paper using a spray coating method at 50 °C on a heating plate with vacuum support. The mass loading of catalyst on the carbon paper was 0.55 mg_{Pt} cm^{-2}.

Physical and Chemical Characterizations

Scanning and transmission electron microscopy were employed to characterize the morphology of the synthesized catalysts, utilizing a Thermo Fisher Scientific Helios 5 CX for SEM and a Talos F200X for HRTEM imaging. Phase composition was revealed through X-ray diffraction (XRD, Malvern Panalytical Empyrean) conducted at 40 kV and 40 mA with Cu Kα radiation. Functional groups were characterized by Fourier-transform infrared spectroscopy (FTIR, Bruker INVENIO S) in attenuated total reflectance (ATR) mode. Surface chemical states were probed via X-ray photoelectron spectroscopy (XPS, Thermo Fisher Scientific Nexsa G2) with monochromatic Al Kα radiation, where all spectra were calibrated to the C 1s peak at 284.8 eV. Surface charge properties were measured by zeta potential analysis (Malvern Panalytical Zetasizer Pro) at 25 °C, while wettability was evaluated with an optical contact angle meter (DataPhysics OCA 25). Finally, the concentration of ions leached during stability testing was determined by inductively coupled plasma-optical emission spectrometry (ICP-OES, Agilent 5110). Raman spectroscopy measurements were conducted employing a Thermo Fisher Scientific DXR3 xi Raman microscope equipped with a 532 nm laser.

In Situ Raman Measurements

For in situ Raman studies, we employed an electrochemical cell (Shanghai Chuxi Industrial Co., Ltd.) containing the as-prepared catalysts (1 × 1 cm^2) as the working electrode, with an Ag/AgCl electrode and a platinum wire ring as the reference and counter electrodes, respectively. During measurements, the electrolyte solution (1.0 M KOH + 0.5 M NaCl) was continuously fed into the cell using a peristaltic pump while Raman spectra were acquired by focusing the laser beam through the quartz window onto the catalyst surface at given potentials.

Electrochemical Characterizations

All electrochemical data were acquired with a CORRTEST CS2350 M bipotentiostat workstation, using a three-electrode cell configuration for OER studies and a two-electrode setup for overall water splitting experiments at room temperature. Electrochemical measurements utilized both three-electrode and two-electrode configurations. The three-electrode cell consisted of a prepared catalyst working electrode, an Ag/AgCl reference (saturated KCl, salt bridge), and a Pt plate counter. The two-electrode cell employed the prepared catalyst and Pt/C as the anode and cathode, respectively. Electrolytes were simulated and natural alkaline seawater solution. For OER activity studies, linear sweep voltammetry (LSV) was conducted at a scan rate of 5 mV s^{-1} after activating the electrode with 25 cyclic voltammetry (CV) cycles. Electrochemical impedance spectroscopy (EIS) measurements were carried out at an overpotential of 250 mV, with a frequency range from 100 kHz to 100 mHz and a perturbing AC amplitude of 5 mV. The obtained EIS data were fitted using *ZView* software. Catalyst stability was evaluated through chronopotentiometry tests at a constant current density of 1.0 A cm^{-2}.

All potentials in this study were reported relative to the reversible hydrogen electrode (RHE), as defined by eq 1 and reported with *iR*-compensation

$$E_{RHE} = E_{Ag/AgCl} + 0.1989 + 0.059 \times pH(25\ ^\circ C) - (i \times R_s) \quad (1)$$

where i and R_s are the current and solution resistance obtained from EIS measurements, respectively.

The overpotential (η) values were calculated according to eq 2.[73]

$$\eta = E_{RHE} - 1.232 \quad (2)$$

The Tafel plots were obtained by plotting η versus log j. The Tafel slopes were extracted by linear regression of the Tafel plots using eq 3.

$$\eta = \pm b \times \log j + a \quad (3)$$

Here, j denotes the current density and b is the Tafel slope (mV dec^{-1}).

The electrochemically active surface area (ECSA) was calculated based on eq 4.[74]

$$ECSA = A_{geo} \times \frac{C_{dl}}{C_s} \quad (4)$$

where A_{geo} denotes the geometric surface area of the electrode, C_{dl} represents the douuble-layer capacitance and C_s is the specific capacitance. The value of C_{dl} was obtained by performing cyclic voltammetry (CV) at different scan rates (20 to 120 mV s^{-1}) in the nonfaradaic region (1.17−1.23 V vs RHE). Based on these measurements, a linear relation of $(j_a - j_c)/2$ against the scan rate values was plotted, and C_{dl} was estimated from the slope of the linear fit. C_s is typically regarded as a constant for Ni-based electrodes in KOH electrolyte (0.040 mF cm^{-2}), consistent with literature values.[62]

The Faradaic efficiency (FE) was calculated using eq 5 based on gas volume measurements by the water drainage method in an H-type electrolysis cell during the electrolysis process.[47,69]

$$FE\% = \frac{n \times F \times V}{Q \times V_m} \times 100 \quad (5)$$

The stoichiometric factor n equals 4 for the OER, corresponding to the number of transferred electrons. The Faraday constant F is 96,485 C mol^{-1}. In the calculation, V represents the measured volume of evolved gas (L), Q is the total electric charge passed (C) during electrolysis, and V_m is the molar volume of gas (24.47 L mol^{-1} at 298.15 K and 1 atm standard conditions).

Electrochemical Corrosion Studies

Corrosion studies were conducted via Tafel polarization techniques to determine the corrosion potential and current. Following stabilization of the open-circuit potential (OCP), measurements were carried out within a potential window of ±250 mV relative to the OCP employing a standard three-electrode cell configuration. The system consisted of the as-synthesized catalyst as the working electrode, a saturated Ag/AgCl reference electrode, and a Pt plate counter electrode.

Hypochlorite Detection

The detection of chlorine species in the electrolyte after the stability test was conducted using the iodimetric titration method. The electrolyte (1.0 mL) was first acidified to pH 1−2 using 0.5 M H_2SO_4. Subsequently, 0.5 mL of 0.5 M KI was added under continuous stirring. A yellow color change occurs if chlorine species are present.[15]

■ ASSOCIATED CONTENT

Supporting Information

The Supporting Information is available free of charge at https://pubs.acs.org/doi/10.1021/acs.jpclett.6c00056.

Additional characterization and electrochemical data, SEM images, TEM images, SAED pattern, inverse FFT patterns, XPS spectra and fitting results, contact angle

https://doi.org/10.1021/acs.jpclett.6c00056
J. Phys. Chem. Lett. 2026, 17, 4828−4838

measurements, LSV curves, CV curves, Raman spectra, in-situ Raman setup, water drainage method for FE% calculation, EIS fitting data, electrochemical corrosion test results and ICP-OES data (PDF)

AUTHOR INFORMATION

Corresponding Authors

Ping Xu − *State Key Laboratory of Space Power-Sources, School of Chemistry and Chemical Engineering, Harbin Institute of Technology, Harbin 150001, China;* orcid.org/0000-0002-1516-4986; Email: pxu@hit.edu.cn

Mir Ghasem Hosseini − *Electrochemistry Research Laboratory, Department of Physical Chemistry, Faculty of Chemistry, University of Tabriz, Tabriz 5166616471, Iran;* orcid.org/0000-0002-3117-8608; Email: mg-hosseini@tabrizu.ac.ir

Kaixi Wang − *Harbin Institute of Technology, Zhengzhou Advanced Research Institute, Zhengzhou 450000, China; National Key Laboratory of Science and Technology on Advanced Composites in Special Environments, Harbin Institute of Technology, Harbin 150001, China;* Email: kaixiwang@hit.edu.cn

Bo Song − *School of Physics, Harbin Institute of Technology, Harbin 150001, China; Harbin Institute of Technology, Zhengzhou Advanced Research Institute, Zhengzhou 450000, China; Laboratory for Space Environment and Physical Sciences, Frontiers Science Center for Matter Behave in Space Environment and National Key Laboratory of Laser Spatial Information, Harbin Institute of Technology, Harbin 150001, China;* orcid.org/0000-0003-2000-5071; Email: songbo@hit.edu.cn

Authors

Vahid Daneshvariesfahlan − *School of Physics, Harbin Institute of Technology, Harbin 150001, China; Harbin Institute of Technology, Zhengzhou Advanced Research Institute, Zhengzhou 450000, China*

Yifei Xu − *National Key Laboratory of Science and Technology on Advanced Composites in Special Environments, Harbin Institute of Technology, Harbin 150001, China*

Shengyu Ma − *School of Physics, Harbin Institute of Technology, Harbin 150001, China*

Qiang Fu − *School of Physics, Harbin Institute of Technology, Harbin 150001, China; Harbin Institute of Technology, Zhengzhou Advanced Research Institute, Zhengzhou 450000, China; Laboratory for Space Environment and Physical Sciences, Frontiers Science Center for Matter Behave in Space Environment, Harbin Institute of Technology, Harbin 150001, China;* orcid.org/0000-0003-1066-2131

Yuming Huang − *Harbin Institute of Technology, Zhengzhou Advanced Research Institute, Zhengzhou 450000, China*

Bing Zhang − *Harbin Institute of Technology, Zhengzhou Advanced Research Institute, Zhengzhou 450000, China*

Jiheng Zhang − *Harbin Institute of Technology, Zhengzhou Advanced Research Institute, Zhengzhou 450000, China*

Yishen Cheng − *Harbin Institute of Technology, Zhengzhou Advanced Research Institute, Zhengzhou 450000, China*

Complete contact information is available at: https://pubs.acs.org/10.1021/acs.jpclett.6c00056

Author Contributions

V.D. and Y.X. contributed equally. The manuscript was written through contributions of all authors. All authors have given approval to the final version of the manuscript.

Notes

The authors declare no competing financial interest.

ACKNOWLEDGMENTS

This work was supported by the National Science Fund for Distinguished Young Scholars (grant no. 52225201), the National Natural Science Foundation of China (grant no. 52271207, 52402242, 52402003, 524B2010), National Key Laboratory of Laser Spatial Information Foundation (LSI2024JCKY01), the Fundamental Research Funds for the Central Universities (grant no. HIT.BRET.2022001), the Postdoctoral Fellowship Program of CPSF (grant no. GZC20242200, GZC20252684), the China Postdoctoral Science Foundation (grant no. 2024M764162, 2025M784364), the Heilongjiang Postdoctoral Fund (LBH-Z24012), the Henan Province Science and Technology Research Project (grant no. 252102241037). The authors also thank the Laboratory Center of Zhengzhou Research Institute, Harbin Institute of Technology.

REFERENCES

(1) Vogt, E. T. C.; Weckhuysen, B. M. The refinery of the future. *Nature* **2024**, *629* (8011), 295−306.

(2) Yang, X.; Nielsen, C. P.; Song, S.; McElroy, M. B. Breaking the hard-to-abate bottleneck in China's path to carbon neutrality with clean hydrogen. *Nat. Energy* **2022**, *7* (10), 955−965.

(3) Ma, S.; Wang, K.; Rafique, M.; Han, J.; Fu, Q.; Jiang, S.; Wang, X.; Yao, T.; Xu, P.; Song, B. Reconstruction of Ferromagnetic/Paramagnetic Cobalt-Based Electrocatalysts under Gradient Magnetic Fields for Enhanced Oxygen Evolution. *Angew. Chem., Int. Ed.* **2024**, *63* (46), No. e202412821.

(4) Guo, B.; Ding, Y.; Huo, H.; Wen, X.; Ren, X.; Xu, P.; Li, S. Recent Advances of Transition Metal Basic Salts for Electrocatalytic Oxygen Evolution Reaction and Overall Water Electrolysis. *Nano-Micro Lett.* **2023**, *15* (1), 57.

(5) Huang, J.; Wang, R.; Sheng, H.; Zhu, X.; Dominic Ross, R.; Hua, D.; Lin, L.; Li, Y.; Zhang, Q.; Gu, L.; Wang, X.; Xu, P.; Lu, J.; Jiang, S.; Han, J.; Song, B.; Jin, S. Isotope-dependent Tafel analysis probes proton transfer kinetics during electrocatalytic water splitting. *Nat. Chem.* **2025**, DOI: 10.1038/s41557-025-01934-5.

(6) Liu, H.; Yao, T.; Ma, S.; Lei, B.; Fu, Q.; Wang, X.; Xu, P.; Song, B. Application and development of PEM water electrolysis technology in the aerospace field. *J. Zhengzhou Univ. Aeronaut* **2025**, *43*, 1.

(7) van der Spek, M.; Banet, C.; Bauer, C.; Gabrielli, P.; Goldthorpe, W.; Mazzotti, M.; Munkejord, S. T.; Røkke, N. A.; Shah, N.; Sunny, N.; Sutter, D.; Trusler, J. M.; Gazzani, M. Perspective on the hydrogen economy as a pathway to reach net-zero CO_2 emissions in Europe. *Energy Environ. Sci.* **2022**, *15* (3), 1034−1077.

(8) Chen, H.; Fan, S.; Song, Q.; Jiang, L.; Chen, Y.; Li, J.; Zhang, X. Preparation of Ni-Doped Mo_2C/C Bifunctional Catalysts and Their Performance in Electrolytic Water Splitting. *J. Synth. Cryst.* **2025**, *54* (1), 158−164.

(9) Sun, X.; Shen, W.; Liu, H.; Xi, P.; Jaroniec, M.; Zheng, Y.; Qiao, S.-Z. Corrosion-resistant NiFe anode towards kilowatt-scale alkaline seawater electrolysis. *Nat. Commun.* **2024**, *15* (1), 10351.

(10) Chen, L.; Yu, C.; Dong, J.; Han, Y.; Huang, H.; Li, W.; Zhang, Y.; Tan, X.; Qiu, J. Seawater electrolysis for fuels and chemicals production: fundamentals, achievements, and perspectives. *Chem. Soc. Rev.* **2024**, *53* (14), 7455−7488.

(11) Li, Z.; Yao, Y.; Sun, S.; Liang, J.; Hong, S.; Zhang, H.; Yang, C.; Zhang, X.; Cai, Z.; Li, J.; Ren, Y.; Luo, Y.; Zheng, D.; He, X.; Liu, Q.; Wang, Y.; Gong, F.; Sun, X.; Tang, B. Carbon Oxyanion Self-

Transformation on NiFe Oxalates Enables Long-Term Ampere-Level Current Density Seawater Oxidation. *Angew. Chem., Int. Ed.* **2024**, *63* (1), No. e202316522.
(12) Zhu, J.; Mao, B.; Wang, B.; Cao, M. The dynamic anti-corrosion of self-derived space charge layer enabling long-term stable seawater oxidation. *Appl. Catal. B: Environ.* **2024**, *344*, 123658.
(13) Zhang, S.; Wang, Y.; Li, S.; Wang, Z.; Chen, H.; Yi, L.; Chen, X.; Yang, Q.; Xu, W.; Wang, A.; Lu, Z. Concerning the stability of seawater electrolysis: a corrosion mechanism study of halide on Ni-based anode. *Nat. Commun.* **2023**, *14* (1), 4822.
(14) Liang, J.; Cai, Z.; Li, Z.; Yao, Y.; Luo, Y.; Sun, S.; Zheng, D.; Liu, Q.; Sun, X.; Tang, B. Efficient bubble/precipitate traffic enables stable seawater reduction electrocatalysis at industrial-level current densities. *Nat. Commun.* **2024**, *15* (1), 2950.
(15) You, H.; Wu, D.; Si, D.; Cao, M.; Sun, F.; Zhang, H.; Wang, H.; Liu, T.-F.; Cao, R. Monolayer NiIr-Layered Double Hydroxide as a Long-Lived Efficient Oxygen Evolution Catalyst for Seawater Splitting. *J. Am. Chem. Soc.* **2022**, *144* (21), 9254−9263.
(16) He, X.; Li, Z.; Yao, Y.; Luo, F.; Sun, X.; Tang, B. Surface and Interfacial Engineering of Electrocatalysts for Seawater Electrolysis. *Acc. Chem. Res.* **2026**, *59* (3), 518−528.
(17) Jin, H.; Xu, J.; Liu, H.; Shen, H.; Yu, H.; Jaroniec, M.; Zheng, Y.; Qiao, S.-Z. Emerging materials and technologies for electrocatalytic seawater splitting. *Sci. Adv.* **2023**, *9* (42), No. eadi7755.
(18) He, X.; Yao, Y.; Zhang, M.; Zhou, Y.; Zhang, L.; Ren, Y.; Dong, K.; Tang, H.; Nan, J.; Zhou, X.; Luo, H.; Ying, B.; Yu, Q.; Luo, F.; Tang, B.; Sun, X. Engineered PW_{12}-polyoxometalate docked Fe sites on CoFe hydroxide anode for durable seawater electrolysis. *Nat. Commun.* **2025**, *16* (1), 5541.
(19) Kuang, Y.; Kenney, M. J.; Meng, Y.; Hung, W.-H.; Liu, Y.; Huang, J. E.; Prasanna, R.; Li, P.; Li, Y.; Wang, L.; Lin, M.-C.; McGehee, M. D.; Sun, X.; Dai, H. Solar-driven, highly sustained splitting of seawater into hydrogen and oxygen fuels. *Proc. Natl. Acad. Sci. U S A* **2019**, *116* (14), 6624−6629.
(20) Kang, X.; Yang, F.; Zhang, Z.; Liu, H.; Ge, S.; Hu, S.; Li, S.; Luo, Y.; Yu, Q.; Liu, Z.; Wang, Q.; Ren, W.; Sun, C.; Cheng, H.-M.; Liu, B. A corrosion-resistant RuMoNi catalyst for efficient and long-lasting seawater oxidation and anion exchange membrane electrolyzer. *Nat. Commun.* **2023**, *14* (1), 3607.
(21) Liu, W.; Yu, J.; Sendeku, M. G.; Li, T.; Gao, W.; Yang, G.; Kuang, Y.; Sun, X. Ferricyanide Armed Anodes Enable Stable Water Oxidation in Saturated Saline Water at 2 A/cm^2. *Angew. Chem., Int. Ed.* **2023**, *62* (40), No. e202309882.
(22) Jadhav, A. R.; Kumar, A.; Lee, J.; Yang, T.; Na, S.; Lee, J.; Luo, Y.; Liu, X.; Hwang, Y.; Liu, Y.; Lee, H. Stable complete seawater electrolysis by using interfacial chloride ion blocking layer on catalyst surface. *J. Mater. Chem. A* **2020**, *8* (46), 24501−24514.
(23) Fan, R.; Liu, C.; Li, Z.; Huang, H.; Feng, J.; Li, Z.; Zou, Z. Ultrastable electrocatalytic seawater splitting at ampere-level current density. *Nat. Sustain.* **2024**, *7* (2), 158−167.
(24) Cheng, J.; Liu, W.; Chen, S.; Zhang, Y.; Cao, A.; Zhang, Y.; Shen, Z.; Yang, Y.; Zhang, Y.; Li, Y.; Zhou, D.; Sun, X. Fluoride-Engineered Electrolyte for Highly Stable and Efficient Alkaline Seawater Electrolysis at 2 A cm^{-2}. *Angew. Chem., Int. Ed.* **2025**, *64* (52), No. e18106.
(25) Ma, T.; Xu, W.; Li, B.; Chen, X.; Zhao, J.; Wan, S.; Jiang, K.; Zhang, S.; Wang, Z.; Tian, Z.; Lu, Z.; Chen, L. The Critical Role of Additive Sulfate for Stable Alkaline Seawater Oxidation on Nickel-Based Electrodes. *Angew. Chem., Int. Ed.* **2021**, *60* (42), 22740−22744.
(26) Pal, S.; Shimizu, K.; Khatun, S.; Singha, S.; Watanabe, S.; Roy, P. Electrolyte engineering for effective seawater splitting based on manganese iron chromium layered triple hydroxides as novel bifunctional electrocatalysts. *J. Mater. Chem. A* **2023**, *11* (23), 12151−12163.
(27) He, X.; Yao, Y.; Zhang, L.; Wang, H.; Tang, H.; Jiang, W.; Ren, Y.; Nan, J.; Luo, Y.; Wu, T.; Luo, F.; Tang, B.; Sun, X. Hexafluorophosphate additive enables durable seawater oxidation at ampere-level current density. *Nat. Commun.* **2025**, *16* (1), 4998.
(28) Chen, S.; Zhuo, Y.; Wang, X.; Li, S.; Lu, J.; Liu, D.; Pan, H.; Wang, Z. Advances of layered double hydroxide electrocatalysts for high-current-density alkaline water/seawater splitting. *Coord. Chem. Rev.* **2024**, *510*, 215832.
(29) Guo, C.; Xu, Y.; Deng, N.; Huang, X. Efficient degradation of organophosphorus pesticides and in situ phosphate recovery via NiFe-LDH activated peroxymonosulfate. *Chem. Eng. J.* **2025**, *524*, 169107.
(30) Zhou, L.; Lan, C.; Xie, R.; Yang, Y.; Qin, F. Preparation and Electrochemical Performance of Flower-Like NiCo-LDH/CB Composite. *J. Synth. Cryst.* **2020**, *49* (12), 2331−2335.
(31) Zhang, B.; Liu, S.; Zhang, S.; Cao, Y.; Wang, H.; Han, C.; Sun, J. High Corrosion Resistance of NiFe-Layered Double Hydroxide Catalyst for Stable Seawater Electrolysis Promoted by Phosphate Intercalation. *Small* **2022**, *18* (45), 2203852.
(32) Lv, L.; Yang, Z.; Chen, K.; Wang, C.; Xiong, Y. 2D Layered Double Hydroxides for Oxygen Evolution Reaction: From Fundamental Design to Application. *Adv. Energy Mater.* **2019**, *9* (17), 1803358.
(33) Wang, Y.; Pan, Q.; Qiao, Y.; Wang, X.; Deng, D.; Zheng, F.; Chen, B.; Qiu, J. Layered Metal Oxide Nanosheets with Enhanced Interlayer Space for Electrochemical Deionization. *Adv. Mater.* **2023**, *35* (15), 2210871.
(34) Li, Z.; Lin, G.; Wang, L.; Lee, H.; Du, J.; Tang, T.; Ding, G.; Ren, R.; Li, W.; Cao, X.; Ding, S.; Ye, W.; Yang, W.; Sun, L. Seed-assisted formation of NiFe anode catalysts for anion exchange membrane water electrolysis at industrial-scale current density. *Nat. Catal.* **2024**, *7* (8), 944−952.
(35) Zhang, J.; Liu, J.; Xi, L.; Yu, Y.; Chen, N.; Sun, S.; Wang, W.; Lange, K. M.; Zhang, B. Single-Atom Au/NiFe Layered Double Hydroxide Electrocatalyst: Probing the Origin of Activity for Oxygen Evolution Reaction. *J. Am. Chem. Soc.* **2018**, *140* (11), 3876−3879.
(36) Tan, L.; Yu, J.; Wang, C.; Wang, H.; Liu, X.; Gao, H.; Xin, L.; Liu, D.; Hou, W.; Zhan, T. Partial Sulfidation Strategy to NiFe-LDH@$FeNi_2S_4$ Heterostructure Enable High-Performance Water/Seawater Oxidation. *Adv. Funct. Mater.* **2022**, *32* (29), 2200951.
(37) Huang, C.; Zhou, Q.; Duan, D.; Yu, L.; Zhang, W.; Wang, Z.; Liu, J.; Peng, B.; An, P.; Zhang, J.; Li, L.; Yu, J.; Yu, Y. The rapid self-reconstruction of Fe-modified Ni hydroxysulfide for efficient and stable large-current-density water/seawater oxidation. *Energy Environ. Sci.* **2022**, *15* (11), 4647−4658.
(38) Li, L.; Dai, Y.; Xu, Q.; Zhang, B.; Zhang, F.; You, Y.; Ma, D.; Li, S.-S.; Zhang, Y.-X. Interlayer expanded nickel-iron layered double hydroxide by intercalation with sodium dodecyl sulfate for enhanced oxygen evolution reaction. *J. Alloys Compd.* **2021**, *882*, 160752.
(39) Carrasco, J. A.; Sanchis-Gual, R.; Silva, A. S.-D.; Abellán, G.; Coronado, E. Influence of the Interlayer Space on the Water Oxidation Performance in a Family of Surfactant-Intercalated NiFe-Layered Double Hydroxides. *Chem. Mater.* **2019**, *31* (17), 6798−6807.
(40) Lin, Y.; Wang, H.; Peng, C.-K.; Bu, L.; Chiang, C.-L.; Tian, K.; Zhao, Y.; Zhao, J.; Lin, Y.-G.; Lee, J.-M.; Gao, L. Co-Induced Electronic Optimization of Hierarchical NiFe LDH for Oxygen Evolution. *Small* **2020**, *16* (38), 2002426.
(41) Viana, R. B.; Da Silva, A. B. F.; Pimentel, A. S. Adsorption of Sodium Dodecyl Sulfate on Ge Substrate: The Effect of a Low-Polarity Solvent. *Int. J. Mol. Sci.* **2012**, *13* (7), 7980−7993.
(42) Li, Y.; Lu, X.; Wu, K.; Yang, L.; Zhang, T.; Wang, F. Exploration the inhibition mechanism of sodium dodecyl sulfate on Mg alloy. *Corros. Sci.* **2020**, *168*, 108559.
(43) Romero Ortiz, G.; Lartundo-Rojas, L.; Samaniego-Benítez, J. E.; Jiménez-Flores, Y.; Calderón, H. A.; Mantilla, A. Photocatalytic behavior for the phenol degradation of ZnAl layered double hydroxide functionalized with SDS. *J. Environ. Manag.* **2021**, *277*, 111399.
(44) Zhang, H.; Li, H.; Akram, B.; Wang, X. Fabrication of NiFe layered double hydroxide with well-defined laminar superstructure as highly efficient oxygen evolution electrocatalysts. *Nano Res.* **2019**, *12* (6), 1327−1331.

https://doi.org/10.1021/acs.jpclett.6c00056
J. Phys. Chem. Lett. 2026, 17, 4828−4838

(45) Xu, Z. P.; Jin, Y.; Liu, S.; Hao, Z. P.; Lu, G. Q. Surface charging of layered double hydroxides during dynamic interactions of anions at the interfaces. *J. Colloid Interface Sci.* **2008**, *326* (2), 522−529.
(46) Kong, Y.; Huang, Y.; Meng, C.; Zhang, Z. Sodium dodecylsulfate-layered double hydroxide and its use in the adsorption of 17β-estradiol in wastewater. *RSC Adv.* **2018**, *8* (55), 31440−31454.
(47) Wang, K.; Wang, S.; Hui, K. S.; Li, J.; Zha, C.; Dinh, D. A.; Shao, Z.; Yan, B.; Tang, Z.; Hui, K. N. Dense Platinum/Nickel Oxide Heterointerfaces with Abundant Oxygen Vacancies Enable Ampere-Level Current Density Ultrastable Hydrogen Evolution in Alkaline. *Adv. Funct. Mater.* **2023**, *33* (8), 2211273.
(48) Zhuo, Y.; Liu, D.; Qiao, L.; Chen, S.; Lu, J.; IP, W. F.; Pan, H.; Wang, Z. Ultrafast Room-Temperature Synthesis of Large-Scale, Low-Cost, and Highly Active Ni-Fe Based Electrodes toward Industrialized Seawater Oxidation. *Adv. Energy Mater.* **2023**, *13* (39), 2301921.
(49) Bo, S.; Zhang, X.; Wang, C.; Wang, H.; Chen, X.; Zhou, W.; Cheng, W.; Liu, Q. Inorganic-organic hybrid cobalt spinel oxides for catalyzing the oxygen evolution reaction. *Nat. Commun.* **2025**, *16* (1), 2483.
(50) Enkhtuvshin, E.; Yeo, S.; Choi, H.; Kim, K. M.; An, B.-S.; Biswas, S.; Lee, Y.; Nayak, A. K.; Jang, J. U.; Na, K.-H.; Choi, W.-Y.; Ali, G.; Chae, K. H.; Akbar, M.; Chung, K. Y.; Yoo, K.; Chung, Y.-C.; Shin, T. H.; Kim, H.; Chung, C.-Y.; Han, H. Surface Reconstruction of Ni-Fe Layered Double Hydroxide Inducing Chloride Ion Blocking Materials for Outstanding Overall Seawater Splitting. *Adv. Funct. Mater.* **2023**, *33* (22), 2214069.
(51) Huang, Y.; Jiang, L.-W.; Shi, B.-Y.; Ryan, K. M.; Wang, J.-J. Highly Efficient Oxygen Evolution Reaction Enabled by Phosphorus Doping of the Fe Electronic Structure in Iron-Nickel Selenide Nanosheets. *Adv. Sci.* **2021**, *8* (18), 2101775.
(52) Shen, W.; Ye, Y.; Hu, Y.; Wu, H.; Xia, Q.; Xie, H.; Li, Z.; Zhang, N.; An, L.; Si, R.; Xi, P.; Yan, C.-H. Corrosion Protection of Rare Earth for Kilowatt-Level Alkaline Seawater Electrolyzer. *J. Am. Chem. Soc.* **2025**, *147* (20), 17190−17200.
(53) Chen, H.; Liu, M.; Jiang, Z.; Sun, S.; Shakir, I.; Hou, S.; Sun, X. Achieving durable alkaline seawater oxidation over NiFe layered double hydroxide via sulfur doping. *Nano Res. Energy* **2025**, *4*, No. e9120211.
(54) Wang, X.; Hu, H.; Song, J.; Ma, J.; Du, H.; Wang, J. J.; Wang, M.; Chen, W.; Zhou, Y.; Wang, J.; Yang, M.; Zhang, L. Surface Anticorrosion Engineering by Polyphosphate Oxyanions for Durable Seawater Oxidation. *Adv. Energy Mater.* **2025**, *15* (4), 2402883.
(55) Zhang, L.; Liang, J.; Yue, L.; Dong, K.; Li, J.; Zhao, D.; Li, Z.; Sun, S.; Luo, Y.; Liu, Q.; Cui, G.; Ali Alshehri, A.; Guo, X.; Sun, X. Benzoate anions-intercalated NiFe-layered double hydroxide nanosheet array with enhanced stability for electrochemical seawater oxidation. *Nano Res. Energy* **2022**, *1*, e9120028.
(56) Wang, H.; Li, Z.; Hong, S.; Yang, C.; Liang, J.; Dong, K.; Zhang, H.; Wang, X.; Zhang, M.; Sun, S.; Yao, Y.; Luo, Y.; Liu, Q.; Li, L.; Chu, W.; Du, M.; Gong, F.; Sun, X.; Tang, B. Tungstate Intercalated NiFe Layered Double Hydroxide Enables Long-Term Alkaline Seawater Oxidation. *Small* **2024**, *20* (28), 2311431.
(57) Kuang, Y.; Kenney, M. J.; Meng, Y.; Hung, W.-H.; Liu, Y.; Huang, J. E.; Prasanna, R.; Li, P.; Li, Y.; Wang, L.; Lin, M.-C.; McGehee, M. D.; Sun, X.; Dai, H. Solar-driven, highly sustained splitting of seawater into hydrogen and oxygen fuels. *Proc. Natl. Acad. Sci. U. S. A* **2019**, *116* (14), 6624−6629.
(58) Gao, T.-Q.; Zhou, Y.-Q.; Zhao, X.-J.; Liu, Z.-H.; Chen, Y. Borate Anion-Intercalated NiV-LDH Nanoflakes/NiCoP Nanowires Heterostructures for Enhanced Oxygen Evolution Selectivity in Seawater Splitting. *Adv. Funct. Mater.* **2024**, *34* (24), 2315949.
(59) Li, Z.; Liang, J.; Hong, S.; Ren, Y.; Zhang, M.; Sun, S.; Cai, Z.; Yang, C.; Wang, H.; Luo, Y.; Liu, S.; Yao, Y.; Gong, F.; Sun, X.; Tang, B. A triple-defense electrocatalyst for robust seawater oxidation. *Nat. Commun.* **2025**, *16* (1), 10327.
(60) Liu, H.; Shen, W.; Jin, H.; Xu, J.; Xi, P.; Dong, J.; Zheng, Y.; Qiao, S.-Z. High-Performance Alkaline Seawater Electrolysis with Anomalous Chloride Promoted Oxygen Evolution Reaction. *Angew. Chem., Int. Ed.* **2023**, *62* (46), No. e202311674.
(61) Qiu, Z.; Tai, C.-W.; Niklasson, G. A.; Edvinsson, T. Direct observation of active catalyst surface phases and the effect of dynamic self-optimization in NiFe-layered double hydroxides for alkaline water splitting. *Energy Environ. Sci.* **2019**, *12* (2), 572−581.
(62) Malek, A.; Xue, Y.; Lu, X. Dynamically Restructuring Ni_xCr_yO Electrocatalyst for Stable Oxygen Evolution Reaction in Real Seawater. *Angew. Chem., Int. Ed.* **2023**, *62* (40), No. e202309854.
(63) Song, Y.; Sun, M.; Zhang, S.; Zhang, X.; Yi, P.; Liu, J.; Huang, B.; Huang, M.; Zhang, L. Alleviating the Work Function of Vein-Like Co_XP by Cr Doping for Enhanced Seawater Electrolysis. *Adv. Funct. Mater.* **2023**, *33* (30), 2214081.
(64) Wu, L.; Yu, L.; Zhang, F.; McElhenny, B.; Luo, D.; Karim, A.; Chen, S.; Ren, Z. Heterogeneous Bimetallic Phosphide Ni_2P-Fe_2P as an Efficient Bifunctional Catalyst for Water/Seawater Splitting. *Adv. Funct. Mater.* **2021**, *31* (1), 2006484.
(65) Wu, L.; Yu, L.; Zhu, Q.; McElhenny, B.; Zhang, F.; Wu, C.; Xing, X.; Bao, J.; Chen, S.; Ren, Z. Boron-modified cobalt iron layered double hydroxides for high efficiency seawater oxidation. *Nano Energy* **2021**, *83*, 105838.
(66) Yu, L.; Wu, L.; McElhenny, B.; Song, S.; Luo, D.; Zhang, F.; Yu, Y.; Chen, S.; Ren, Z. Ultrafast room-temperature synthesis of porous S-doped Ni/Fe (oxy)hydroxide electrodes for oxygen evolution catalysis in seawater splitting. *Energy Environ. Sci.* **2020**, *13* (10), 3439−3446.
(67) Wu, L.; Yu, L.; McElhenny, B.; Xing, X.; Luo, D.; Zhang, F.; Bao, J.; Chen, S.; Ren, Z. Rational design of core-shell-structured CoP_x@FeOOH for efficient seawater electrolysis. *Appl. Catal. B: Environ.* **2021**, *294*, 120256.
(68) Enkhtuvshin, E.; Yeo, S.; Choi, H.; Kim, K. M.; An, B.-S.; Biswas, S.; Lee, Y.; Nayak, A. K.; Jang, J. U.; Na, K.-H.; Choi, W.-Y.; Ali, G.; Chae, K. H.; Akbar, M.; Chung, K. Y.; Yoo, K.; Chung, Y.-C.; Shin, T. H.; Kim, H.; Chung, C.-Y.; Han, H. Surface Reconstruction of Ni-Fe Layered Double Hydroxide Inducing Chloride Ion Blocking Materials for Outstanding Overall Seawater Splitting. *Adv. Funct. Mater.* **2023**, *33* (22), 2214069.
(69) Chen, Y.; Liu, Y.; Zhai, W.; Liu, H.; Sakthivel, T.; Guo, S.; Dai, Z. Metastabilizing the Ruthenium Clusters by Interfacial Oxygen Vacancies for Boosted Water Splitting Electrocatalysis. *Adv. Energy Mater.* **2024**, *14* (21), 2400059.
(70) Patil, S. A.; Khot, A. C.; Chavan, V. D.; Rabani, I.; Kim, D.-k.; Jung, J.; Im, H.; Shrestha, N. K. Electrostatically robust CoFeOF nanosheet against chloride for green-H_2 production in alkaline seawater electrolysis. *Chem. Eng. J.* **2024**, *480*, 146545.
(71) Cai, Z.; Liang, J.; Li, Z.; Yan, T.; Yang, C.; Sun, S.; Yue, M.; Liu, X.; Xie, T.; Wang, Y.; Li, T.; Luo, Y.; Zheng, D.; Liu, Q.; Zhao, J.; Sun, X.; Tang, B. Stabilizing NiFe sites by high-dispersity of nanosized and anionic Cr species toward durable seawater oxidation. *Nat. Commun.* **2024**, *15* (1), 6624.
(72) Ma, W.; Li, D.; Liao, L.; Zhou, H.; Zhang, F.; Zhou, X.; Mo, Y.; Yu, F. High-Performance Bifunctional Porous Iron-Rich Phosphide/Nickel Nitride Heterostructures for Alkaline Seawater Splitting. *Small* **2023**, *19* (19), 2207082.
(73) Qi, L.; Gao, Y.; Gao, Y.; Zheng, Z.; Luan, X.; Zhao, S.; Chen, Z.; Liu, H.; Xue, Y.; Li, Y. Controlled Growth of Metal Atom Arrays on Graphdiyne for Seawater Oxidation. *J. Am. Chem. Soc.* **2024**, *146* (8), 5669−5677.
(74) Sun, F.; Qin, J.; Wang, Z.; Yu, M.; Wu, X.; Sun, X.; Qiu, J. Energy-saving hydrogen production by chlorine-free hybrid seawater splitting coupling hydrazine degradation. *Nat. Commun.* **2021**, *12* (1), 4182.

https://doi.org/10.1021/acs.jpclett.6c00056
J. Phys. Chem. Lett. 2026, 17, 4828−4838